

1 Automatic knot detection and measurements from
2 X-ray CT images of wood: A review and validation of
3 an improved algorithm on softwood samples

4 Longuetaud F.^{a,b,*}, Mothe F.^{a,b}, Kerautret B.^c, Krähenbühl A.^c, Hory L.^c,
5 Leban J.M.^d, Debled-Rennesson I.^c

6 ^a*INRA, UMR1092 LERFoB, 54280 Champenoux, France*

7 ^b*AgroParisTech, UMR1092 LERFoB, 54000 Nancy, France*

8 ^c*LORIA, UMR CNRS 7503, Université de Nancy*
9 *Campus Scientifique, 54506 Vandœuvre-lès-Nancy Cedex, France*

10 ^d*ENSTIB, 88051 Epinal, France*

11 **Abstract**

12 An algorithm to automatically detect and measure knots in CT images of
13 softwood beams was developed. The algorithm is based on the use of 3D con-
14 nex components and a 3D distance transform constituting a new approach
15 for knot diameter measurements.

16 The present work was undertaken with the objective to automatically and
17 non-destructively extract the distributions of knot characteristics within trees.
18 These data are valuable for further studies related to tree development and
19 tree architecture, and could even contribute to satisfying the current demand
20 for automatic species identification on the basis of CT images.

21 A review of the literature about automatic knot detection in X-ray CT images
22 is provided. Relatively few references give quantitatively accurate results of
23 knot measurements (i.e., not only knot localisation but knot size and incli-
24 nation as well).

25 The method was tested on a set of seven beams of Norway spruce and silver

*Corresponding author
Preprint submitted to Elsevier

March 29, 2012

Email addresses: longueta@nancy.inra.fr (Longuetaud F.),
mothe@nancy.inra.fr (Mothe F.), Bertrand.Kerautret@iutds.uhp-nancy.fr
(Kerautret B.), adrien057@gmail.com (Krähenbühl A.), yabb85@gmail.com (Hory L.),
Jean-Michel.Leban@enstib.uhp-nancy.fr (Leban J.M.),
Isabelle.Debled-Rennesson@loria.fr (Debled-Rennesson I.)

26 fir. The outputs were compared with manual measurements of knots per-
27 formed on the same images.

28 The results obtained are promising, with detection rates varying from 71 to
29 100%, depending on the beams, and no false alarms were reported. Particu-
30 lar attention was paid to the accuracy obtained for automatic measurements
31 of knot size and inclination. Comparison with manual measurements led to
32 a mean R^2 of 0.86, 0.87, 0.59 and 0.86 for inclination, maximum diameter,
33 length and volume, respectively.

34 *Keywords:* Branchiness, 3D distance transform, Computer tomography,
35 *Picea abies, Abies alba*

36 1. Introduction

37 Wood knots are the prolongation within the tree stem of the branches. By
38 linking the living crown where photosynthesis occurs, to the pith of the main
39 stem and, finally, to the roots where the mineral nutrients are assimilated,
40 branches and knots play a vital role in tree physiology. However, despite the
41 fact that trees without branches do not exist, wood users would nevertheless
42 like to obtain knot free lumbers. The frequency and size of the apparent knots
43 are probably the first depreciation factors considered by wood suppliers for
44 estimating the price of timber. This is also one of the main criteria considered
45 in the visual grading of lumber.

46 The occurrence of knots within a piece of wood has several technolog-
47 ical drawbacks, principally due to the deviation of the grain angle in and
48 around the knots. Wood can be considered as an orthotropic material whose
49 properties differ drastically along and across the grain. For example, the lon-

50 longitudinal modulus of elasticity (along the grain) is typically ten times higher
51 than the transverse one. From a mechanical point of view, this means that a
52 knot within a wood beam may be assimilated to a hole. In wood machining,
53 the quality of the surface around the knots is often depreciated due to the
54 grain deviation while the life expectancy of tools may be severely shortened
55 by shocks against the knots. Finally, knots usually depreciate the aesthetic
56 quality of the wood as well.

57 Knowledge of knot geometry and location would be valuable in a sawmill
58 for optimising cutting decisions or improving the grading of logs or lumber.
59 CT scanners designed expressly for the wood industry are now available and
60 some of the largest sawmills are now equipped with them. Such data are
61 needed for studying tree architecture (Colin et al., 2010; Heuret et al., 2002;
62 Passo et al., 2002; Meredieu and Caraglio, 1998), pruning (Seifert et al.,
63 2010; Hein, 2008), branchiness (Colin and Houllier, 1991, 1992; Kershaw
64 et al., 2009; Weiskittel et al., 2010; Courbet et al., 2007; Moberg, 1999;
65 Meredieu et al., 1998) and knot morphology (Lemieux et al., 2001; Björk-
66 lund and Petersson, 1999; Björklund, 1997; Lemieux et al., 1997; Samson
67 et al., 1996; Samson, 1993). Branch and knot models for various species have
68 been included into simulators for assessing wood quality (Houllier et al., 1995;
69 de Coligny et al., 2003; Ikonen et al., 2009).

70 Observation of branch scars may help to assess the quality of a log but is
71 not sufficient to predict its knottiness. Many knots linked to branches that
72 were artificially or naturally pruned several years earlier may remain deeply
73 hidden within the stem, notably at the lower part of old trees. Moreover, the
74 knot shape from the outer branch insertion to the stem pith is a matter of

75 guesswork.

76 X-ray computer tomography has been recognised as being the most promis-
77 ing method to non-destructively analyse the internal structure of logs (Hailey
78 and Morris, 1987; Chang, 1992; Schad et al., 1996). A review of the existing
79 methods for automatically measuring knottiness on the basis of CT images
80 is presented in the next section.

81 The objective of this paper was to propose an entirely automated method
82 able to inventory knots from X-ray CT images of a piece of wood (round
83 wood or beam) and to obtain data on knot geometry without any human in-
84 tervention. Even if execution time was considered in the algorithmic choices,
85 no special effort was devoted to speed optimisation. The first step of the
86 algorithm, image segmentation, was not studied in details since a simple
87 thresholding operation was efficient in the present case. On the contrary,
88 special attention was paid to the validation step. Validation was performed
89 on a large set of 428 knots using two software tools dedicated to (i) man-
90 ual measurement of the knot shape on the CT images, and (ii) automatic
91 matching of the manually measured and automatically detected knots. The
92 challenges were to maximise the knot detection rate, to minimise the false
93 alarms and to obtain an accurate and complete knot geometric description
94 (including location, diameter, volume, inclination and shape descriptors).

95 The knot detection software was published under the GPL license and
96 made available to the public (<http://www.loria.fr/equipes/adage/3DKnotDM>).

97 **2. Review of existing methods to non-destructively and automati-**
98 **cally measure knottiness on the basis of CT images**

99 This section is dedicated to the state of the art with respect to exist-
100 ing algorithms of knot detection based on the analysis of X-ray CT images.
101 This review does not include some studies based on low-resolution images (for
102 example, obtained from only two or three X-ray projections) performed in or-
103 der to be more compatible with normal sawing speed (e.g., Pietikäinen, 1996;
104 Flood et al., 2003). Indeed, comparison of accuracies with high-resolution
105 images would have been of limited interest.

106 The first approaches of knot detection based on X-ray CT images found
107 in the literature were developed in the 1980s.

108 Taylor et al. (1984) gave some general ideas for the detection of knots but
109 without describing an algorithm in detail.

110 The first detailed description of an algorithm was given by Funt (1985),
111 followed by Funt and Bryant (1987). A thresholding of the grey level his-
112 togram based on derivative methods was used to classify the pixels into four
113 classes, where knots belong to the class with the highest density. Potential
114 knot components were then represented by convex regions, and their size and
115 orientation were analysed by the system in order to check whether they cor-
116 responded to actual knots or not: (i) components that were too small were
117 eliminated on the basis of a size criterion; (ii) the orientation of each region
118 was compared with the axis that passed through the pith and the centre of
119 gravity of the region. Indeed, branches are connected to the stem pith where
120 they have their biological origin and principal knot axes pass approximately
121 through the pith. The 3D aspect of CT image stacks was not used in this

122 approach and the authors do not give validation results.

123 In the 1990s an Australian research team proposed several interesting and
124 original approaches for segmenting knots (Wells et al., 1991; Som et al., 1993,
125 1995; Davis et al., 1996), even if they do not seem to have finalised them.
126 Validation results are therefore not provided.

127 A first approach (Wells et al., 1991) was based on vectors of statistical cri-
128 teria computed in 5×5 neighbourhoods and on statistical methods applied
129 to these vectors, such as principal component analysis.

130 A second approach (Som et al., 1993) consisted in applying edge detection
131 and processing the resulting image with a 3×3 mask adapted to the radial
132 structure of knots: if the local edge was oriented perpendicularly to a virtual
133 line passing through the pith, then the pixel of interest was removed.

134 A third approach (Som et al., 1993) was based on subtractions of pairs of
135 consecutive CT images. This method makes it possible to detect moving com-
136 ponents such as knots from one CT image to another. A similar approach was
137 used by Jaeger et al. (1999). This method is particularly efficient to remove
138 sapwood when it is present. However, the method is strongly dependent on
139 knot size and inclination and on the distance between two consecutive CT
140 images (Longuetaud, 2005).

141 In a fourth approach (Som et al., 1995), the authors used mathematical mor-
142 phology to detect breaks in the annual growth ring structure.

143 Zhu et al. provided an interesting algorithm based on a system of rules
144 for defect detection in logs. They first applied low-level operations (filtering
145 with a 3D Unser filter to eliminate annual rings and to preserve important
146 image details, segmentation using a multi-thresholding scheme for 2D com-

147 ponent identification, 3D volume growing) (Zhu et al., 1991b,a), followed by
148 a high-level module (Zhu et al., 1991c,d), which consisted in a rule-based
149 expert system for defect recognition. After selecting some features of inter-
150 est (e.g., grey level mean value, distance to the centre of the log, volume),
151 the authors computed confidence values for these features, depending on the
152 wood characteristics. In Zhu et al. (1996), this part of the algorithm was
153 refined by using the Dempster-Shafer theory of evidential reasoning. Visual
154 results are provided for CT images of red oak and yellow poplar, but the
155 authors do not give quantified accuracy results. Zhu and Beex (1994) tested
156 another approach based on the application of spatial autoregressive modelling
157 to wood-grain texture analysis.

158 Another original approach was developed by Grundberg and Grönlund
159 (1992) for Scots pine logs. The main objective was to develop knot models¹
160 in order to reduce the amount of data to be handled in their database (the
161 Swedish Stem Bank) by saving only the model parameters obtained from
162 automatic knot detection rather than pixel values. A low-pass filter was first
163 applied to remove annual growth rings. The originality of the method was to
164 work on concentric surfaces centred on the pith (manually detected) within
165 logs (i.e., similar to surfaces obtained by rotary cutting logs). Knots were de-
166 tected by thresholding (fixed threshold: 875 kg.m^{-3}) five concentric surfaces
167 located in the heartwood and by analysing overlapping between successive
168 surfaces. The location of knots in the sapwood was predicted (not detected)
169 by using models based on the previous detections in the heartwood. Vali-

¹Models to predict tangential and longitudinal diameters and positions as functions of the radial distance to the pith.

170 dation results are given based on 177 knots from five trees. The size and
171 location of knots that were predicted on the most external concentric surface
172 in the sapwood were compared with manual measurements. For their best
173 tested model, five knots were missed, and means and standard deviations (SD
174 in brackets) of predicted minus real knot diameters were -2.55 (4.74) mm in
175 the tangential direction and -8.77 (8.76) mm in the longitudinal direction.
176 Oja validated and adapted the previous algorithm for Norway spruce on two
177 stems (Oja, 1996) and then applied it to 12 logs (Oja, 2000). In addition,
178 he provided some results about the detection of the sound knot/dead knot
179 border. In this work, 80 to 100% of the knots larger than 7 mm were detected
180 (94% in average). Nine false knots were found in the 12 logs. The detection
181 of knots was assessed by comparing real CT images and reconstructed CT
182 images on the basis of the automatically estimated knot parameters. The
183 accuracy of diameter measurements (at the dead knot border) was assessed
184 on 27 knots based on comparisons between measurements on real boards
185 and on reconstructed boards. The mean and SD of predicted (measured on
186 reconstructed boards) minus real (measured on real boards) knot diameters
187 were - 2 (3) mm.
188 Nordmark (2003) later extended the Swedish Stem Bank with knot parame-
189 ters estimated from knot detection in CT images of young Scots pine trees.
190 The segmentation of knots in CT images (first step of the algorithm) was
191 done by using the Artificial Neural Network (ANN) (see details below). Then,
192 similarly to the previous associated works, concentric surfaces were used to
193 identify knots in 3D and to fit knot models for size and position. The accu-
194 racy of the extracted descriptions was evaluated by comparing the size and

195 position of knots measured on ten real boards from three trees with corre-
196 sponding boards reconstructed on the basis of the descriptions. A total of
197 84% of 185 real knots was detected. The average and SD differences between
198 simulated and real diameters in tangential and longitudinal directions were
199 0.6 (4.0) mm and -0.6 (3.9) mm, respectively.

200 In these studies, the CT slice thickness was 5 mm and the distance between
201 two consecutive slices was 5 mm for pine logs and 10 mm for spruce logs
202 and young pine logs. The resolution was approximately $1.37 \text{ mm}\cdot\text{pixel}^{-1}$ for
203 young pine logs.

204 In our opinion, Bhandarkar et al. (1996; 1999) gave the most finalised
205 algorithm that we found in the literature. The first step consisted in the
206 segmentation of CT images in four pixel classes (the knots belonged to the
207 class with the highest density) by using a complex form of an area-based mul-
208 tiple thresholding algorithm. The algorithm then located the pith, grouped
209 the pixels of the segmented images on the basis of their 2D connectivity
210 (region-growing process), deleted regions that were too small, and classified
211 each 2D region as a defect-like or defect-free region by computing shape,
212 orientation and morphological features (considering, for example, like Funt
213 and Bryant (1987), that knot principal axes pass approximately through the
214 stem pith). 2D regions were then represented by convex hulls, and holes
215 were filled. Finally, the 2D regions with adequate 3D support were labelled
216 as true defects. Knot parameters such as knot inclination and slenderness
217 were then computed from these 3D regions and helped to remove invalid knot
218 regions. White ash, red oak, black walnut and hard maple logs were anal-
219 ysed. Defects were manually identified and delineated in colour images of

220 real cross-sections to enable comparisons with the corresponding automatic
221 detections in CT images. The numbers of knots considered were 225, 161,
222 330 and 194 for white ash, red oak, black walnut and hard maple, respec-
223 tively. Detection rates were between 80.8% for red oak and 89.3% for white
224 ash, and false alarm rates were between 5.1% for red oak and 12.7% for hard
225 maple. Localisation accuracies were given in terms of centroid displacement,
226 orientation difference and overlap factor.

227 More recently, Bhandarkar et al. (2006; 2008) proposed a novel approach
228 based on Kalman filter-based tracking algorithms. The defects were simul-
229 taneously detected, classified, localised and reconstructed in 3D. The results
230 were promising with detection rates of 100% obtained for white ash, hard
231 maple and red oak logs.

232 Andreu and Rinnhofer (2003a; 2003b) proposed a method to detect knots
233 in CT images of Norway spruce logs. Like Grundberg and Grönlund (1992)
234 earlier, they aimed to represent knots by parametric functions. First, the
235 pith was detected in CT images. Then, a multi-modal histogram threshold-
236 ing method was applied to classify the pixels into four classes, after several
237 image pre-processing steps (e.g., annual ring structure removal by Gaus-
238 sian filtering). The 2D knot areas that were detected on successive images
239 were then grouped together, based on their distance to the pith and the
240 direction of their principal axis in the CT image plane, in order to obtain
241 a 3D support from which knot models were fitted (3D curve along which
242 the 2D cross-section is swept). The validation was done based on four logs
243 by making comparisons between knots that were visible on real boards and
244 on corresponding virtual boards obtained on the basis of the knot models.

245 For knots larger than 10 mm, the detection and false alarm rates averaged
246 96% and 10%, respectively. If all knots were considered, these rates were
247 73% and 13%, respectively. Accuracy results for angular position, elevation
248 position and diameter were 1.9 (2.9) °, 0.9 (10.4) mm and 0.7 (10.1) mm,
249 respectively². In this study, CT slices were taken every 20 mm and the pixel
250 resolution was 1.55 mm × 1.55 mm.

251 More recently, Aguilera et al. (2008b; 2008a) proposed a novel approach
252 based on active contours for the detection of wood characteristics (which
253 included knots) in CT images. They defined the system constraints on the
254 basis of *a priori* information about the characteristics to be detected. They
255 tested their algorithm on *Pinus radiata* CT images and the results seemed to
256 be promising from the visual point of view. However, they did not provide
257 quantitative validation results.

258 Baumgartner et al. (2010) proposed an algorithm for 2D knot detec-
259 tion and measurements and validated it on 21 knots from two Scots pine
260 logs. First, they used slightly adapted versions of algorithms developed by
261 Longuetaud et al. for pith detection (Longuetaud et al., 2004) and heart-
262 wood/sapwood boundary detection (Longuetaud et al., 2007). Then, for
263 the knot detection in heartwood, they applied a thresholding, hole filling
264 and some morphological operations and, last, they identified connex com-
265 ponents as being knots. Validation (provided in graphical form) was done
266 for azimuthal positions and maximal diameters of knots by comparison with
267 manual measurements performed on corresponding real cross-sections.

²These figures are probably means and SD of differences in "automatic minus manual measurements", but this was not specified by the authors.

268 Other approaches based on classification methods focused mainly on the
269 segmentation of knots (and often other wood characteristics) in CT images.
270 The results were then expressed as percentages of correctly classified pixels.
271 Hagman and Grundberg (1995) tested two classification methods (back-
272 propagation Artificial Neural Network (ANN) and Partial Least Squares
273 modelling) in order to separate knots from clearwood in CT images and to
274 distinguish between four types of knots (sound knots in sapwood, dry knots
275 in sapwood, sound knots in heartwood and rotten knots in sapwood). The
276 accuracies were between 85% and 97% of correctly classified pixels (based on
277 163 knots). The two methods tested gave equal results.

278 Li et al. (1996), He (1997) and Schmoltdt et al. (1996; 1998b; 1998a) also
279 used a back-propagation ANN to detect wood characteristics in CT images
280 of two species of oak (*Quercus rubra* L. and *Quercus nigra* L.), yellow poplar
281 and black cherry. For each pixel in the image, the network took the values
282 of pixels in 5×5 2D or in $3 \times 3 \times 3$ 3D neighbourhoods as input, as well as
283 the distance of the target pixel to the centre of the log. Species-dependent
284 and species-independent classifiers were tested. As output, the target pixel
285 was associated with a wood characteristic (which included knots). All tested
286 classifiers had accuracies above 90% (above 95% for all species-dependent
287 classifiers). Improvements by post-processing based on mathematical mor-
288 phology were suggested by the authors and one specific approach was pro-
289 posed by Sarigul et al. (2003).

290 Nordmark also used feed-forward back-propagation ANN for segmenting knots
291 in CT images of a 30-year-old Scots pine (Nordmark, 2002). The objective
292 was to enlarge the Swedish Stem Bank with young trees with a small propor-

293 tion of heartwood because the algorithm previously described by Grundberg
294 and Grönlund (1992) was not adapted to that case. ANN was used here as
295 the first step of a more complete algorithm including parametrical descrip-
296 tions of knots (Nordmark, 2003) (see above). The ANN was trained using
297 five images taken at different heights from each of five trees. The ANN in-
298 puts were a 9×9 neighbourhood, oriented in the radial direction, and the
299 distance of the target pixel to the pith (manually located). They obtained
300 $95.9\% \pm 1.2\%$ of correctly classified pixels (cross-validation method).
301 Rojas et al. (2005; 2006) tested two parametric supervised classification al-
302 gorithms to detect wood characteristics in sugar maple logs: a minimum
303 distance classifier (MDC) and a maximum likelihood classifier (MLC). They
304 used five logs (1.5 m long) from one single freshly cut tree (group 1) and
305 three logs from a sawmill yard (group 2). A total of 125 and 90 CT images
306 were analysed for group 1 and 2, respectively. Confusion between coloured
307 heartwood and knots was observed for both groups. It should be noted that
308 the authors were more interested in detecting sapwood (for which accura-
309 cies were better) than knots because it is a key factor for determining sugar
310 maple lumber value. The overall accuracies were 83.1% (MDC) and 82.6%
311 (MLC) for group 1 (evaluation of 25 CT images), and 76.4% (MDC) and
312 78.0% (MLC) for group 2. Regarding knots, correctly classified pixels were
313 64.8% (MDC) and 61% (MLC) for group 1, and 47.4% (MDC) and 44.7%
314 (MLC) for group 2. The slice thickness was 5 mm and the resolution was
315 between 0.6 and 0.9 mm.pixel⁻¹.
316 More recently, Wei et al. (2008a; 2008b; 2009) tested both back-propagation
317 ANN and MLC in order to identify internal wood characteristics (which in-

318 cluded knots) in sugar maple and black spruce logs. They tested a faster
319 converging algorithm for the ANN. Nine image features were used as input
320 of both classifiers: grey level values, the distance between the pixel of interest
321 and the pith, and seven textural features (homogeneity, contrast, dissimilar-
322 ity, mean, SD, entropy and angular second moment). The validation was
323 done by comparison with manually delineated characteristics in 20 CT im-
324 ages (Wei et al., 2009). The overall accuracies for the MLC classifier and
325 for the ANN were 80.9% (78.3% for knots) and 97.6% (95.5% for knots),
326 respectively (Wei et al., 2009).

327 **3. Materials and methods**

328 *3.1. Sampling*

329 The knot detection software was applied to a set of seven squared beams
330 (25 cm × 25 cm × 300 cm) of silver fir (*Abies alba* Mill.) and Norway
331 spruce (*Picea abies* (L.) Karst.). The beams, courtesy of the sawmill, Ets.
332 Siat-Braun (Alsace, France), were selected at random in the lumber yard in
333 which the two species are undifferentiated. After macroscopic identification,
334 it was found that there were four beams of fir (#1 to #4) and three beams
335 of spruce (#5 to #7). The beams were air-dried several weeks before the
336 measurements were taken.

337 *3.2. CT scanning*

338 The samples were analysed using an X-ray scanner device (BrightSpeed
339 Excel by GE Healthcare) designed for medical use. The piece of wood is
340 translated at approximately 2 cm/s across a ring (gantry) around which

341 the X-ray tube and the detector rotate. A volumetric reconstruction of the
342 sample is delivered almost instantaneously in the form of a stack of $512 \times$
343 512 images. The grey-level images are expressed in Hounsfield units that
344 may be converted to wood density by simple linear regression (Freyburger
345 et al., 2009). In the present study, six of the seven beams were scanned
346 with the X-ray generator set to 120 kV - 50 mA, and a slice thickness and
347 interval between slices of 3.75 mm. Beam #1 was previously scanned with
348 the generator set to 120 kV - 80 mA, the slice thickness to 1.25 mm, and
349 the interval between slices to 1 mm (which means that there was overlapping
350 between slices). For cost reasons, beam #1 was not scanned again with
351 exactly the same settings as the six other beams. The image reconstruction
352 of the beams was performed using a DETAIL filter³ with a pixel size of 0.74
353 mm \times 0.74 mm. Since the scanner can only process 1.50 m-long pieces, the
354 beams were scanned in two passes.

355 *3.3. Manual knot measurements*

356 The knot shape and size were manually recorded using ImageJ software
357 (Rasband, 2010) and a plug-in dedicated to the analysis of internal tree archi-
358 tecture by X-ray CT scanning (*Gourmands* plug-in described in Colin et al.
359 (2010)). The operator reviews the image stack and manually places markers
360 along both sides of each branch, starting from the pith and progressing to-
361 wards the external end. The distance between the two lines of markers gives
362 the diameter profile of the knot in the plane perpendicular to the main axis
363 of the beam, assuming a circular cross section. The trajectory of the pith

³One of the seven reconstruction filters available with the scanner software.

364 is also recorded using specific markers. The software makes it possible to
365 compute and export the geometrical description of each measured knot. The
366 following variables were used in this study to characterise each knot:

- 367 • Starting point (SP) and end point (EP): first marker near the pith and
368 mid-point of the last two markers;
- 369 • Length: distance from SP to EP;
- 370 • Inclination: angle between the horizontal plane and the SP to EP line⁴;
- 371 • Azimuth: horizontal angle between a given axis and the SP to EP line;
- 372 • Maximum diameter;
- 373 • Volume: estimated by summing the volumes of truncated cones defined
374 by the marker lines.

375 These measurements are subjective. The operator has to decide which
376 singularities correspond to a knot and the exact location of the knot bound-
377 aries. For the purpose of standardising the measurements, the operator was
378 asked to only consider knots for which pith (the secondary pith of the branch)
379 was visible and to adjust the grey-level contrast to a fixed range (-1000 to
380 +200 Hounsfield units).

381 Figure 1 illustrates the variability encountered in the samples studied for
382 knot size and shape.

383 *****Figure 1 about here*****

⁴assuming that the beam longitudinal axis is vertical

384 *3.4. Algorithm for automatic knot detection and measurements*

385 *3.4.1. Description*

386 • Data input

387 The images created by a medical CT scanner device are stored in Di-
388 CoM format with grey levels expressed in Hounsfield numbers (H),
389 which are calibrated in such a way that Hounsfield numbers measured
390 on air and water have a value of -1000 and 0, respectively.

391 • Pith detection

392 An initial thresholding with a fixed value of -700 H ($\simeq 300 \text{ kg.m}^{-3}$) was
393 applied for removing the background. The pith was then detected on
394 each CT image of a beam by using the algorithm described in Longue-
395 taud et al. (2004). Briefly, the algorithm is based on a Hough transform
396 method and virtually draws lines perpendicular to the annual growth
397 rings, looking for a maximum of accumulation with respect to the num-
398 ber of intersecting lines. The pith location is estimated by linear inter-
399 polation in CT images including knots, for which no clear maximum of
400 accumulation is found.

401 • Knot segmentation

402 A thresholding was used to segment knots. The threshold value was
403 selected based on the grey level histogram, smoothed by Loess local
404 polynomial fitting, by searching for the rightmost minimum or inflexion
405 point in a region ranging from -300 to 100 H ($\simeq 700$ to 1100 kg.m^{-3}).

406 • Connex components (3D)

407 Since the memory size of the whole 3D image can be very large, we
408 defined a strategy that made it possible to save memory space while
409 maintaining efficient extraction of connected components. The 3D im-
410 age was processed slice-by-slice while maintaining the set of connected
411 components in memory.

412 *****Figure 2 about here*****

413 Figure 2 illustrates the main idea of the algorithm. Only the current
414 and previous slices (represented in red) are stored in the system mem-
415 ory. From each processed voxel (in blue), the list of connected com-
416 ponents is maintained by analysing the 26-connected neighbourhood
417 (illustrated in cyan).

418 • Processing of each component:

419 – Convex hull (2D)

420 The Graham scan algorithm was used to compute the convex hull
421 of the pixels belonging to the component in each slice. A hole-
422 filling algorithm was then applied to fill the polygons.

423 – Distance transform (3D)

424 The distance transform applied to a 3D space makes it possible to
425 compute the minimal distance between any point and the object
426 surface. To perform such a transformation, the algorithm of Saito
427 and Toriwaki (1994) was applied to each connected component.

428 An example of a distance transform is illustrated in Fig. 3 with
429 a real knot. The points around the surface of the object are at
430 distances close to 0, represented in shades of red, while the farthest
431 points are represented in shades of blue.

432 *****Figure 3 about here*****

433 – Principal component analysis (3D)

434 The three inertia axes of the component were computed by apply-
435 ing a principal component analysis to the set of 3D coordinates of
436 the voxels belonging to the component.

437 3.4.2. Outputs

438 For each 3D component, the following data were computed (Fig. 4):

- 439 ● Starting and end points: 3D coordinates of the first and last points of
440 the component projection onto the principal inertia axis. The starting
441 point is the closest to the pith;
- 442 ● Length: distance from the starting point to the end point;
- 443 ● Inclination: angle between the horizontal plane and the principal inertia
444 axis⁵. Mathematically, it ranges from -90° to 90° . A null value means
445 that the component is horizontal; inclination is positive or negative
446 when the component goes up or down, respectively;

⁵Assuming that the beam longitudinal axis is vertical.

- 447 • Elongation: ratio between the second and first eigenvalues of the 3D
448 principal component analysis. Mathematically, it ranges from 0 to 1
449 with values close to 0 for very elongated components;
- 450 • Radial deviation angle (RDA): angle between the horizontal projection
451 of the principal inertia axis and the horizontal axis linking tree pith
452 to the centre of gravity of the component. Mathematically, it ranges
453 from -90° to 90° . A null value means that the component has a radial
454 orientation; values near 90° or -90° mean that the component axis is
455 perpendicular to the radial direction;
- 456 • Azimuth: angle between the horizontal projection of the principal in-
457 ertia axis and a given horizontal axis in the beam coordinate system;
- 458 • Maximum diameter: maximal value of the distance-transformed com-
459 ponent;
- 460 • Volume: product of the number of voxels belonging to the component
461 with the volume of a voxel;

462 *****Figure 4 about here*****

463 On the basis of these output variables, some criteria were established in
464 order to identify the 3D components corresponding to actual knots. Details
465 about criteria computation are given in Section 3.5.

466 3.4.3. Software implementation

467 The *3DKnotDM* software was implemented in C++ language and was
468 tested on different platforms such as *Linux* and *Mac OS X*. Several common

469 libraries were included in the development to perform efficient functionality.
470 The main architecture is based on the QT (2011) Development Frameworks,
471 which was combined with the use of the LibQGLViewer (2011) library for
472 the 3D display part. The DiCoM image files were read using the Grassroots
473 library (Malaterre, 2008). The Armadillo library (Sanderson, 2010) was used
474 to process the 3D image matrix and to perform the 3D principal component
475 analysis. Finally, the DGtal (2011) library was also included to perform
476 efficient surface extraction from the discrete set of surface elements (surfels).

477 *3.5. Calibration and statistical validation*

478 A cross-validation approach of the "leave-one-out" type was used. The
479 3D components of one single beam were used as the validation data set and
480 the knots of the six other beams as the calibration data set. The procedure
481 was repeated until each beam had been used as a validation data set.

482 *3.5.1. Calibration*

483 The calibration procedure mainly consisted in defining criterion bounds
484 for deciding whether an automatically detected 3D component was a knot or
485 not.

486 Three criteria were used and were defined on the basis of the biologic
487 knowledge about knots: inclination, elongation and RDA of the 3D compo-
488 nents (details about the computation are given in Section 3.4.2). Spruce and
489 fir knots are slightly tilted and preferentially up oriented. Knots are charac-
490 terised by an elongated shape. Biologically, knots are connected to the pith
491 and their principal axis intersects the pith line.

492 First, the observations used for calibration were defined as the 3D com-
493 ponents belonging to the calibration data set that most likely corresponded
494 to actual knots. This was done by searching the 3D component, when it ex-
495 isted, that was the closest to each manually delineated knot within a window
496 40° wide in azimuth (20° on each side of the actual knot) and 40 mm high
497 in the longitudinal direction (20 mm above and below the actual knot). In
498 addition, among these components, only the ones with diameter and inclina-
499 tion sufficiently close to the manual measurements were retained. This was
500 done by computing the corresponding residuals and by removing the 3D com-
501 ponents whose residuals were identified as outliers. Outliers were detected
502 on the basis of the classical criterion used in the boxplot statistical method
503 (Zuur et al., 2010). The 3D components for which the corresponding pith
504 location was not correctly detected were removed, based on the same crite-
505 rion. Finally, the number of observations used for calibration are indicated
506 in Table 1 for each single beam when it was used for validation.

507 The second step was to define upper bounds for each criterion based on
508 the calibration observations. Statistical distributions were fitted from the ob-
509 served distributions of the criteria. The theoretical distributions were chosen
510 on the basis of their shape and support. Our goal was to approximate the
511 maximal possible value of each criterion. A Weibull distribution (support on
512 $[0; +\infty[)$ was fitted to the absolute value of the tangent of the inclination.
513 The absolute value was used because the signed value would have depended
514 on the beam orientation, which is not always easy to assess (Fig. 1), partic-
515 ularly in the case of an industrial process. A beta distribution (support on
516 $[0; 1])$ was fitted to the elongation criterion. Once again, a Weibull distri-

517 bution was fitted to the absolute value of the tangent of the RDA. For each
518 criterion, based on the fitted distribution, the quantile corresponding to $p =$
519 0.999 was chosen as the upper bound. Table 1 gives the upper bounds that
520 were obtained from the calibration data sets and then used on the respective
521 validation data sets. For an application of the algorithm to other logs or
522 beams, the upper bounds would be the means of the values given in Table
523 1 for the seven beams. Hence, the overall upper bounds would be: 53.1° for
524 the inclination, 0.25 for the elongation criterion and 15.9° for the RDA.

525 *****Table 1 about here*****

526 3.5.2. Validation

527 The observations used for validation were defined as being the 3D compo-
528 nents belonging to the validation data set that had been identified as being
529 knots by the algorithm based on the three criteria described above. For vali-
530 dation purposes, it was necessary to establish a correspondence with manual
531 knot measurements. This was done by searching the 3D component, when
532 it existed, that was the closest to each manually delineated knot within a
533 window 40° wide in azimuth and 40 mm high in the longitudinal direction.

534 The validation of the algorithm was performed on the basis of several cri-
535 teria and aimed at both quantitatively and qualitatively assessing the knot
536 detection . We were interested in the percentage of detected knots and in
537 the rate of false alarms, depending on the knot size. We were also interested
538 in the measurement accuracy for the following variables that were available
539 among the manual measurements: inclination, maximum diameter, length
540 and volume. Since the correspondences between automatic and manual de-
541 tections were looked for within windows restricted in azimuth and height, it

542 would not have been relevant to analyse the accuracy for azimuth and height
543 of insertion. For assessing accuracy, the following criteria were computed:
544 r-square (R^2), root-mean-square error (RMSE), mean of errors (i.e., auto-
545 matic minus manual measurements) and standard deviation of errors. Plots
546 of manual measurements vs. automatic measurements were drawn for each
547 variable by tree species (Mayer and Butler, 1993).

548 R statistical software was used for all computations included in Section
549 3.5 (R Development Core Team, 2009).

550 4. Results

551 4.1. Detection rate

552 Table 2 shows the detection rates observed for each beam. Depending on
553 the sample, 71 to 100% of the measured knots were detected (85% over the
554 whole data set). Figure 5 shows an example of a correctly detected whorl of
555 knots.

556 *****Table 2 about here*****

557 *****Figure 5 about here*****

558 The observation of the 63 missing knots showed that only five of them
559 were really missing in the set of components delivered by the algorithm.
560 In the other cases, a component was actually delivered but either (i) not
561 associated with the measured knot (one case only), or (ii) not identified as a
562 knot due to the merging of several knots within the same component. Knot
563 merging was observed near the pith for 21 knots, 15 of which belonged to
564 beam #7, probably due to the presence of denser compression wood around

565 the pith (Fig. 6). Merging was also observed for 28 knots of beams #3
566 and #4 due to wet areas (Fig. 7). In both cases, the merged components
567 were logically rejected with respect to the elongation or orientation criteria,
568 resulting in lower detection rates.

569 *****Figure 6 about here*****

570 *****Figure 7 about here*****

571 The fourth column of Table 2 gives the number of components that were
572 considered as knots by the automatic algorithm but not associated with a
573 manually measured knot. Careful observation of the CT slices showed that
574 all of the 149 supplemental components actually corresponded to a knot or
575 a bud trace. In most cases, the knot was not measured because of its small
576 size; some other knots were measured but delivered several fragments from
577 which only one was associated with the knot.

578 Figure 8 shows the distributions of detected knots (manually measured
579 or not) and missing detections by diameter classes. In particular, it may be
580 observed that the algorithm was able to detect more knots than the operator
581 for the smallest diameters. Indeed, the operator was asked not to measure
582 the very small branches for which the pith was not visible. The proportion
583 of missing detections was relatively low, regardless of the diameter class.

584 *****Figure 8 about here*****

585 *4.2. Detection accuracy*

586 The accuracy of the automatic measurements was analysed on the basis
587 of the 365 detected knots for which manual measurements were available.

588 The variables that were considered for accuracy were: inclination, maxi-
589 mum diameter, length and volume of knots.

590 Figure 9 shows plots of manual vs. automatic measurements for each of
591 these four variables compared to the $Y=X$ line. R^2 , RMSE, mean of errors
592 and standard deviation of errors are given for each single beam in Table 3.

593 Regarding inclination measurements, the mean RMSE was 4.5° . The re-
594 sults were globally satisfactory with a mean R^2 of 0.86. The least accurate
595 results were obtained for beam #6 with a RMSE of 6.9° and inclinations
596 underestimated by the algorithm, especially for the two branches that were
597 the most bottom oriented. Like beams #1 and #7, beam #6 had the partic-
598 ularity of having its knots quite horizontal and even bottom oriented (Fig.
599 1).

600 Regarding the diameter measurements, the mean RMSE was 3.4 mm.
601 The results were globally satisfactory with a mean R^2 of 0.87. The least
602 accurate results were obtained for beams #6 and #7 with RMSE of 5.3 and
603 4.4 mm, respectively. This was due to the biggest branches for which the
604 maximum diameter was underestimated by the algorithm. In addition, a
605 slight bias was observed for most of the beams, with automatically measured
606 diameters often smaller than the manually measured ones. Beam #6 had
607 the particularity of having bigger knots than the other beams and a quite
608 high variability of knot maximum diameters. The averages of mean errors
609 and standard deviations were -1.8 (2.9) mm.

610 Regarding the length measurements, the mean RMSE was 3.3 cm. This
611 was the variable that was the least accurately measured by the algorithm,
612 with a mean R^2 of 0.59. The least accurate results were obtained for beam

613 #2 with a RMSE of 5.2 cm. A bias was observed for all of the beams since
614 automatically measured lengths were generally shorter than the manually
615 measured ones. Figure 10 shows that the biggest errors essentially occurred
616 for knots with small diameters that sometimes led to fragmented 3D compo-
617 nents due to the thresholding.

618 Regarding the volume measurements, the RMSE for all the beams to-
619 gether was 12.0 cm³. The results were satisfactory with a mean R² of 0.86,
620 except for beam #7 (RMSE of 20.0 cm³), essentially due to two branches for
621 which the volumes were overestimated by the algorithm.

622 For knot diameter and length, no difference in accuracy was observed
623 between spruce and fir. For knot inclination and volume, the results were
624 slightly better for fir than for spruce (statistically assessed by t-tests).

625 The moisture content of the beams (not controlled here) was probably an
626 important factor in relation to the accuracy of the automatic measurements
627 since wood density was similar for knots and wet wood areas, which led to
628 some problems in the automatic detection.

629 *****Figure 9 about here*****

630 *****Table 3 about here*****

631 *****Figure 10 about here*****

632 5. Discussion

633 When aiming to analyse the distributions of knot characteristics within
634 trees (e.g., Colin and Houllier, 1992; Kershaw et al., 2009; Weiskittel et al.,
635 2010), it is particularly important to identify and accurately measure each

636 knot individually. Such data are particularly valuable for studying tree de-
637 velopment and tree architecture, and for linking tree growth conditions to
638 wood quality. In addition, there is a demand for the development of au-
639 tomatic methods of species identification on the basis of various markers
640 measurable in stacks of CT images. Possible markers could include knot dis-
641 tribution within the stem, knot size, inclination and density. Since a simple
642 grey level thresholding was effective for segmenting the knots, we decided
643 to focus our efforts in this study on the identification of individual knots
644 and on the validation of knot detection and measurements. On the other
645 hand, many references found in the literature focus on the segmentation of
646 CT images alone (which would be the first step of a more complete knot
647 detection algorithm) without ultimately providing a method to detect each
648 knot individually. The accuracy results are therefore presented in the form
649 of percentages of correctly classified pixels, which are not easy to interpret
650 by the end-users.

651 The percentage of detected knots (detection rate) is a more powerful
652 criterion that is widely used in studies about individual knot detection. It is
653 important to associate this rate with the corresponding percentage of false
654 alarms (i.e., the number of invalid detections divided by the total number
655 of detected knots). Our detection rates (obtained on the basis of a total
656 of 428 manually detected knots) ranged between 71 and 100%, depending
657 on the beam (85% for all beams together), with no false alarms (i.e., all
658 the 3D components identified as being knots by the algorithm were actual
659 knots, even if they were not all manually measured), which was comparable
660 to the results found in the literature (see Section 2). Our algorithm was

661 particularly efficient for detecting even small branches while maintaining a
662 zero false alarm level.

663 Relatively few validation results are available in the literature with respect
664 to the automatic measurement of knots, especially their size and inclination.
665 This specific point was particularly emphasized in this study. Diameter is
666 the most widely measured and studied knot characteristic. A total of four
667 references provided quantitative results for diameter measurements (Grund-
668 berg and Grönlund, 1992; Oja, 2000; Nordmark, 2003; Andreu and Rinnhofer,
669 2003a). However, validation methods were highly variable (see Section 2).
670 In the present work, we obtained error means and SD of -1.8 (2.9) mm,
671 which could be considered to be very accurate. No quantitative results were
672 found in the literature regarding knot inclination, length or volume measure-
673 ments. The accuracies obtained by applying our algorithm for the automatic
674 measurements of inclination and volume were satisfactory. The knot length
675 measurement was the least accurate. As shown in Section 4, this lack of
676 accuracy generally occurred for small-diameter knots that could lead to frag-
677 mented 3D components due to the thresholding. Some improvements such as
678 a radial dilatation of the 3D components toward the outside of the stem or
679 the connexion of the 3D components on the basis of their azimuth could solve
680 most of the problems. These ideas have not yet been tested in the present
681 version of our algorithm.

682 As reported above, some authors (Oja, 2000; Nordmark, 2003; Andreu
683 and Rinnhofer, 2003a; Baumgartner et al., 2010) validated their algorithm by
684 comparison with manual measurements made on real boards or cross-sections.
685 We chose to validate our results by comparison with manual measurements

686 performed on original CT images. The reason is that we consider that the
687 comparison between knot borders visible on colour images (i.e., based on
688 wood colour variations) and on corresponding CT images (i.e., based on
689 wood density variations) is a distinct problem, totally independent of the
690 algorithm performance, and which should be studied separately.

691 In our study, the manual measurements of knot diameters were performed
692 on CT images, i.e., in a transversal plane, whereas the automatic measure-
693 ments were performed by using the 3D distance transform method that gave
694 the minimum diameter at the knot profile location where the diameter was
695 maximum. That implies to hypothesize that the knot section is circular
696 or larger in the longitudinal direction than in the transverse direction. For
697 Norway spruce, a ratio of 1.057 between diameters measured vertically and
698 horizontally was reported by Merkel (1967) in Skovsgaard (1988), which rep-
699 resents a very slight ovality.

700 Finally, regardless of the type of images being dealt with, manual mea-
701 surements are prone to subjectivity. Although knots are easily visible on
702 images, it is not easy to accurately determine the borders between knots and
703 the surrounding wood (Nordmark, 2005).

704 It should be observed that the use of the 3D distance map offers other po-
705 tential geometric feature extractions such as the knot diameter profile. Such
706 a feature could be available after defining a surface tracking algorithm (by
707 using, for example, the tracking discrete surface algorithm from the DGtal
708 (2011) library) and by focusing on the principal inertia axis.

709 In the current version of the algorithm, the inclination was defined as
710 the angle between the horizontal plane and the line linking the starting point

711 and the end point of the knot, both for manual and automatic measurements.
712 This definition was totally satisfactory in relation to the way the inclination
713 was used in this study, whereas it is questionable from a biological point of
714 view since it depends on the length of the knot and on the stem diameter.
715 The definitions that are often used in existing biological studies about the
716 distribution of knot inclinations within trees (e.g., Colin et al., 1993; Makinen
717 and Colin, 1998; Achim et al., 2006) are questionable for similar reasons: the
718 branch inclination is measured outside of the stem for practical reasons and
719 therefore depends on the stem diameter. CT image analysis makes it possible
720 to non-destructively investigate the inner part of the stem, and it would be
721 more relevant to measure inclination in the first part of the knot that is not
722 visible outside of the stem. In further versions of the algorithm, additional
723 definitions of the inclination will be added to the outputs.

724 A question arose about the sensitivity of our algorithm to the longitudi-
725 nal and transversal resolutions of CT images. For example, Schmoldt et al.
726 (1998b) compared the results obtained with an artificial neural network for
727 two transversal resolutions of 1 mm/pixel and 3 mm/pixel. No significant
728 difference was observed. In our case, the results obtained for beam #1 are
729 better than for the other beams. This could be due to the fact that beam
730 #1 was scanned with a longitudinal resolution about three times better than
731 the other beams. This specific point should be further investigated by scan-
732 ning some materials with different resolutions and by comparing the results
733 of the knot detection, but it has not yet been done due to cost and time
734 considerations.

735 The detection failures due to the merging of several knots within the

736 same component at the location of their connexion to the tree pith could be
737 easily solved by using a black circular mask of 10 mm in diameter around the
738 pith. Indeed, among the 21 knots that were not detected because they were
739 connected together at the pith location (Section 4.1), 20 could be detected by
740 using such a mask, leading to a detection rate of 91% on average (compared
741 to 85% without using the circular mask). However, this method is quite
742 rough, depending on the mask diameter, and more subtle methods should
743 exist, perhaps based on skeletonisation, in order to find the location where
744 the knots are connected together.

745 Several authors (e.g., Funt and Bryant, 1987; Andreu and Rinnhofer,
746 2003a; Nordmark, 2005; Rojas et al., 2006; Wei et al., 2009) encountered diffi-
747 culties in detecting knots in the presence of high moisture content or sapwood
748 (when it was visible) on CT images, especially when knots were connected
749 to sapwood because of comparable density levels. This major problem is still
750 unresolved in the literature. For example, Rojas et al. (2007) demonstrated
751 the effect of moisture content on the accuracy of sapwood detection in sugar
752 maple logs. In our study, the material was not fresh, but some remaining
753 areas of high moisture content led to the merging of several knots within the
754 same 3D component. Longuetaud (2005) proposed a method to overcome
755 this problem but without actual implementation. Further developments of
756 our algorithm will be devoted to this specific problem with the objective of
757 applying the algorithm to fresh beams or logs.

758 Since cross-validation was used in this study, the method was not applied
759 to a true independent validation sample. Nevertheless a small log (approx-
760 imately 15 cm in diameter \times 100 cm in length, taken from a 30-year-old spruce

761 tree) for which the manual measurements were available was processed using
762 the overall upper bounds given in the Materials and Methods section. The
763 results were quite satisfactory since 73 of the 74 knots measured in this log
764 were successfully detected without any false alarm. The R^2 between manual
765 and automatic measurements was 0.94, 0.96, 0.34 and 0.91 for knot inclina-
766 tion, maximal diameter, length and volume, respectively. The results were
767 particularly accurate for maximal diameter, with an error mean and SD of
768 0.0 (0.9) mm.

769 **6. Conclusion**

770 A fully automated algorithm was developed for the detection of knots
771 within silver fir and Norway spruce beams or logs. The detection was non-
772 destructive since it was based on the analysis of CT images acquired by a
773 medical X-ray CT scanner. The algorithm detected and measured knots
774 directly in 3D, based on a connex component analysis and a 3D distance
775 transform.

776 The algorithm was able to detect a total of 85% of 428 knots in seven sil-
777 ver fir and Norway spruce beams (91% when applying a special process to
778 disconnect knots when they were connected together at the pith location).
779 Particular attention was paid to the automatic measurements of knot char-
780 acteristics: inclination, diameter, length and volume. The comparison with
781 manual measurements resulted in an R^2 of 0.86, 0.87, 0.59 and 0.86 for incli-
782 nation, maximum diameter, length and volume, respectively.

783 This study could be extended in the future to solve the problem of the connec-
784 tion of knot components together at the pith location or due to the presence

785 of an area of high moisture content, to validate and adapt the algorithm to
786 other species, and to apply the algorithm to whole stems in order to study
787 the distribution of knot characteristics within trees.

788 **References**

789 Achim, A., Gardiner, B., Leban, J. M., Daquitaine, R., 2006. Predicting the
790 branching properties of Sitka spruce grown in Great Britain. *New Zealand*
791 *Journal of Forestry Science* 36 (2/3).

792 Aguilera, C., Sanchez, R., Baradit, E., 2008a. Detection of knots using X-ray
793 tomographies and deformable contours with simulated annealing. *Wood*
794 *Research* 53 (2), 57–66.

795 Aguilera, C., Sanchez, R., Baradit, E., 2008b. Internal wood inspection with
796 active contour using data from CT scanning. *Wood Research* 53 (4), 13–22.

797 Andreu, J. P., Rinnhofer, A., 2003a. Modeling knot geometry in Norway
798 spruce from industrial CT images. In: Bigün, J., Gustavsson, T. (Eds.),
799 *Proceedings of Image Analysis, 13th Scandinavian Conference (SCIA)*. Vol.
800 2749 of *Lecture Notes in Computer Science*. Springer-Verlag Berlin, Halm-
801 stad, Sweden, pp. 786–791.

802 Andreu, J. P., Rinnhofer, A., 2003b. Modeling of internal defects in logs for
803 value optimization based on industrial CT scanning. In: *Fifth International*
804 *Conference on Image Processing and Scanning of Wood*. Bad Waltersdorf,
805 Austria, pp. 141–150.

- 806 Baumgartner, R., Brüchert, F., UH, S., 2010. Knots in CT scans of Scots
807 pine logs. In: *The Future of Quality Control for Wood & Wood Products*,
808 4-7th May 2010, Edinburgh The Final Conference of COST Action E53.
- 809 Bhandarkar, S., Faust, T. D., Tang, M., 1996. A system for detection of
810 internal log defects by computer analysis of axial CT images. In: *Third*
811 *IEEE Workshop on Applications of Computer Vision WACV'96*. Sarasota,
812 Florida, USA, pp. 258–263.
- 813 Bhandarkar, S. M., Faust, T. D., Tang, M., 1999. CATALOG: a system for
814 detection and rendering of internal log defects using computer tomography.
815 *Machine Vision and Applications* 11 (4), 171–190.
- 816 Bhandarkar, S. M., Luo, X. Z., Daniels, R., Tollner, E. W., 2006. A novel
817 feature-based tracking approach to the detection, localization, and 3-D
818 reconstruction of internal defects in hardwood logs using computer tomog-
819 raphy. *Pattern Analysis and Applications* 9 (2-3), 155–175.
- 820 Bhandarkar, S. M., Luo, X. Z., Daniels, R. F., Tollner, E. W., 2008. Au-
821 tomated planning and optimization of lumber production using machine
822 vision and computed tomography. *Ieee Transactions on Automation Sci-*
823 *ence and Engineering* 5 (4), 677–695.
- 824 Björklund, L., 1997. The interior knot structure of *Pinus sylvestris* stems.
825 *Scandinavian Journal of Forest Research* 12 (4), 403–412.
- 826 Björklund, L., Petersson, H., 1999. Predicting knot diameter of *Pinus*
827 *sylvestris* in Sweden. *Scandinavian Journal of Forest Research* 14 (4), 376–
828 384.

- 829 Chang, S., September 1992. External and internal defect detection to opti-
830 mize cutting of hardwood logs and lumber. Tech. rep.
- 831 Colin, F., Houllier, F., 1991. Branchiness of Norway spruce in north-eastern
832 France: modelling vertical trends in maximum nodal branch size. *Annales*
833 *des Sciences Forestieres* 48, 679–693.
- 834 Colin, F., Houllier, F., 1992. Branchiness of Norway spruce in northeastern
835 France: predicting the main crown characteristics from usual tree mea-
836 surements. *Annales des Sciences Forestieres* 49, 511–538.
- 837 Colin, F., Houllier, F., Joannes, H., Haddaoui, A., 1993. A model of the
838 vertical distribution of diameters, angles and numbers of branches of three
839 *Picea abies* provenances. *Silvae Genetica* 42 (4/5).
- 840 Colin, F., Mothe, F., Freyburger, C., Morisset, J.-B., Leban, J.-M., Fontaine,
841 F., 2010. Tracking rameal traces in sessile oak trunks with X-ray computer
842 tomography: biological bases, preliminary results and perspectives. *Trees-*
843 *structure and Function* 24 (5), 953–967.
- 844 Courbet, F., Sabatier, S., Guedon, Y., 2007. Predicting the vertical location
845 of branches along Atlas cedar stem (*Cedrus atlantica* Manetti) in relation
846 to annual shoot length. *Annals of Forest Science* 64 (7), 707–718.
- 847 Davis, J., Som, S., Svalbe, I., Grant, J., Gold, E., Tsui, K., Wells, P., 1996.
848 The Glass Log Project: grade evaluation and defect location using X-ray
849 computed tomography. In: 14th World Conference on Non-Destructive
850 Testing. Vol. Vol. 3, pages 1423 - 1426. *Trends in NDE Science and Tech-*
851 *nology*, New Delhi.

- 852 de Coligny, F., Ancelin, P., Cornu, G., Courbaud, B., Dreyfus, P., Gore-
853 aud, F., Gourlet-Fleury, S., Meredieu, C., Saint-Andre, L., 2003. CAPSIS:
854 Computer-aided projection for strategies in silviculture: Advantages of
855 a shared forest-modelling platform. In: Amaro, A., Reed, D., Soares, P.
856 (Eds.), Modelling Forest Systems. IUFRO 4 01; IUFRO 4 11, pp. 319–
857 323, workshop on Interface between Reality, Modelling and the Parameter
858 Estimation Process, Sesimbra, Portugal, Jun. 02-05, 2002.
- 859 DGtal, 2011. DGtal: Digital geometry tools and algorithms library. <http://liris.cnrs.fr/dgtal>.
860
- 861 Flood, K., Danielsson, P.-E., Seger, M. M., 2003. On 3D segmentation of
862 knots in 3D-volume data acquired from X-ray linear cone-beam scanning.
863 In: Fifth International Conference on Image Processing and Scanning of
864 Wood. Bad Waltersdorf, Austria, pp. 151–160.
- 865 Freyburger, C., Longuetaud, F., Mothe, F., Constant, T., Leban, J.-M., 2009.
866 Measuring wood density by means of X-ray computer tomography. *Annals*
867 *of Forest Science* 66 (8).
- 868 Funt, B. V., 1985. A computer vision system that analyzes CT-scans of
869 sawlogs. In: *Proceedings of IEEE Conference on Computer Vision and*
870 *Pattern Recognition*. San Francisco, California, pp. 175–177.
- 871 Funt, B. V., Bryant, E. C., 1987. Detection of internal log defects by au-
872 tomatic interpretation of computer tomography images. *Forest Products*
873 *Journal* 37 (1), 56–62.

- 874 Grundberg, S., Grönlund, A., 1992. Log scanning - extraction of knot geome-
875 try. In: The 1st International Seminar/Workshop on Scanning Technology
876 and Image Processing on Wood. Skellefteå, Sweden.
- 877 Hagman, P. O. G., Grundberg, S. A., 1995. Classification of Scots pine (*Pinus*
878 *sylvestris*) knots in density images from CT scanned logs. *Holz Als Roh-*
879 *Und Werkstoff* 53 (2), 75–81.
- 880 Hailey, J. R., Morris, P. I., 1987. Application of scanning and imaging tech-
881 niques to assess decay and wood quality in logs and standing trees. In:
882 Application of scanning and imaging techniques to assess decay and wood
883 quality in logs and standing trees. Forestry Canada/Alberta Forest Service
884 (Canada-Alberta Forest Resource Development Agreement), Edmonton,
885 Alberta Canada, p. 48.
- 886 He, J., 1997. A comparison of artificial neural network classifiers for analysis
887 of CT images for the inspection of hardwood logs. Master thesis.
- 888 Hein, S., 2008. Knot attributes and occlusion of naturally pruned branches
889 of *fagus sylvatica*. *Forest Ecology and Management* 256 (12), 2046–2057.
- 890 Heuret, P., Barthelemy, D., Guedon, Y., Coulmier, X., Tancre, J., 2002.
891 Synchronization of growth branching and flowering processes in the south
892 american tropical tree *Cecropia obtusa* (Cecropiaceae). *American Journal*
893 *of Botany* 89 (7), 1180–1187.
- 894 Houllier, F., Leban, J., Colin, F., JUN 1995. Linking growth modeling to
895 timber quality assessment for Norway spruce. *Forest Ecology and Manage-*
896 *ment* 74 (1-3), 91–102.

- 897 Ikonen, V.-P., Kellomaki, S., Peltola, H., 2009. Sawn timber properties of
898 Scots pine as affected by initial stand density, thinning and pruning: a
899 simulation based approach. *Silva Fennica* 43 (3), 411–431, 6th IUFRO
900 Workshop on Connection between Forest Resources and Wood Quality,
901 Koli Natl Pk, Joensuu, Finland, Jun. 08-14, 2008.
- 902 Jaeger, M., Leban, J.-M., Borianne, P., Chemouny, S., Saint-André, L., 1999.
903 3D stem reconstruction from CT scan exams. From log external shape to
904 internal structures. In: Workshop IUFRO. La Londe-Les-Maures.
- 905 Kershaw, Jr., J. A., Benjamin, J. G., Weiskittel, A. R., 2009. Approaches
906 for modeling vertical distribution of maximum knot size in black spruce:
907 A comparison of fixed- and mixed-effects nonlinear models. *Forest Science*
908 55 (3), 230–237.
- 909 Lemieux, H., Beaudoin, M., Zhang, S., 2001. Characterization and modeling
910 of knots in black spruce (*Picea mariana*) logs. *Wood and Fiber Science*
911 33 (3), 465–475.
- 912 Lemieux, H., Samson, M., Usenius, A., 1997. Shape and distribution of knots
913 in a sample of *Picea abies* logs. *Scandinavian Journal of Forest Research*
914 12, 50–56.
- 915 Li, P., Abbott, A. L., Schmoldt, D. L., 1996. Automated analysis of CT im-
916 ages for the inspection of hardwood logs. In: The 1996 IEEE International
917 Conference on Neural Networks (ICNN). Washington, DC, USA.
- 918 LibQGLViewer, 2011. LibQGLViewer Library. [http://www.libqglviewer.](http://www.libqglviewer.com)
919 [com](http://www.libqglviewer.com).

- 920 Longuetaud, F., 2005. Détection et analyse non destructive de caractéris-
921 tiques internes de billons d'Épicéa commun (*Picea abies* (L.) KARST.)
922 par tomographie à rayons X. Doctoral thesis.
- 923 Longuetaud, F., Leban, J.-M., Mothe, F., Kerrien, E., Berger, M.-O., 2004.
924 Automatic detection of pith on CT images of spruce logs. *Computers and*
925 *Electronics in Agriculture* 44 (2), 107–119.
- 926 Longuetaud, F., Mothe, F., Leban, J.-M., 2007. Automatic detection of
927 the heartwood/sapwood boundary within Norway spruce (*Picea abies* (L.)
928 Karst.) logs by means of CT images. *Computers and Electronics in Agri-*
929 *culture* 58 (2), 100–111.
- 930 Makinen, H., Colin, F., 1998. Predicting branch angle and branch diame-
931 ter of Scots pine from usual tree measurements and stand structural in-
932 formation. *Canadian Journal of Forest Research-Revue Canadienne De*
933 *Recherche Forestiere* 28 (11), 1686–1696.
- 934 Malaterre, M., 2008. GDCM Reference Manual. [http://gdcm.](http://gdcm.sourceforge.net/gdcm.pdf)
935 [sourceforge.net/gdcm.pdf](http://gdcm.sourceforge.net/gdcm.pdf), 1st Edition.
- 936 Mayer, D. G., Butler, D. G., 1993. Statistical validation. *Ecological Modelling*
937 68 (1-2), 21–32.
- 938 Meredieu, C., Caraglio, Y., 1998. Cernes manquants et houppier vivant chez
939 le pin laricio (*Pinus nigra* Arn. ssp. *laricio* (Poir.) Maire). *Canadian Journal*
940 *of Botany-revue Canadienne De Botanique* 76 (12), 2051–2060.
- 941 Meredieu, C., Colin, F., Herve, J., 1998. Modelling branchiness of Corsican

- 942 Pine with mixed-effect models (*Pinus nigra* Arnold ssp. *laricio* (Poiret)
943 Maire). *Annales des Sciences Forestières* 55 (3), 359–374.
- 944 Merkel, O., 1967. Der Einfluss des Baumabstandes auf die Aststärke der
945 Fichte. *Allgemeine Forst Und Jagdzeitung* 138, 113–125.
- 946 Moberg, L., 1999. Variation in knot size of *Pinus sylvestris* is in two initial
947 spacing trials. *Silva Fennica* 33 (2), 131–144.
- 948 Nordmark, U., 2002. Knot identification from CT images of young *Pinus*
949 *sylvestris* sawlogs using artificial neural networks. *Scandinavian Journal of*
950 *Forest Research* 17 (1), 72–78.
- 951 Nordmark, U., 2003. Models of knots and log geometry of young *Pinus*
952 *sylvestris* sawlogs extracted from computed tomographic images. *Scandi-*
953 *navian Journal of Forest Research* 18, 168–175.
- 954 Nordmark, U., 2005. Value recovery and production control in the forestry-
955 wood chain using simulation technique. Doctoral thesis, l'auteur parle des
956 difficultés de la détection des noeuds dans l'aubier par seuillage (il cite
957 d'autres auteurs qui ont souligné cette difficulté tels que Andreu et Flood)
958 mais parle de la capacité de l'oeil humain de distinguer les noeuds dans
959 l'aubier. C'est pourquoi il s'oriente vers une méthode par réseau de neu-
960 rones.
- 961 Oja, J., 1996. Validation of knot models on Norway spruce. In: Second
962 IUFRO Workshop WP S 5.01-04. "Connection between silviculture and
963 wood quality through modelling approaches and simulation software".
964 South Africa.

- 965 Oja, J., 2000. Evaluation of knot parameters measured automatically in CT-
966 images of Norway spruce (*Picea abies* (L.) Karst.). *Holz als Roh- und*
967 *Werkstoff* 58 (5), 375 – 379.
- 968 Passo, A., Puntieri, J., Barthelemy, D., 2002. Trunk and main-branch devel-
969 opment in *Nothofagus pumilio* (Nothofagaceae): a retrospective analysis
970 of tree growth. *Canadian Journal of Botany* 80 (7), 763–772.
- 971 Pietikäinen, M., 1996. Detection of knots in logs using x-ray imaging. Ph.D.
972 thesis.
- 973 QT, 2011. Qt Development Frameworks. <http://qt.nokia.com>.
- 974 R Development Core Team, 2009. R: A language and environment for statis-
975 tical computing. R Foundation for Statistical Computing, Vienna, Austria,
976 ISBN 3-900051-07-0.
977 URL <http://www.R-project.org>
- 978 Rasband, W., 2010. ImageJ. U. S. National Institutes of Health, Bethesda,
979 Maryland, USA, <http://rsb.info.nih.gov/ij>.
980 URL <http://rsb.info.nih.gov/ij>
- 981 Rojas, G., 2005. Détection des défauts internes dans les billes d’Erable à
982 sucre à l’aide d’un scanner à rayons X. Doctoral thesis.
- 983 Rojas, G., Beauregard, R., Hernandez, R. E., Verret, D., Condal, A., 2007.
984 Effect of moisture content variation on CT image classification to identify
985 internal defects of sugar maple logs. *Forest Products Journal* 57 (4), 38–43.

- 986 Rojas, G., Condal, A., Beauregard, R., Verret, D., Hernandez, R. E., 2006.
987 Identification of internal defect of sugar maple logs from CT images using
988 supervised classification methods. *Holz Als Roh-Und Werkstoff* 64 (4), 295–
989 303.
- 990 Saito, T., Toriwaki, J.-I., 1994. New algorithms for euclidean distance
991 transformation of an n-dimensional digitized picture with applications.
992 *Pattern Recognition* 27 (11), 1551 – 1565.
993 URL [http://www.sciencedirect.com/science/article/
994 B6V14-48MPN3T-19S/2/e696034f9dc2c99356a49beeb111b91d](http://www.sciencedirect.com/science/article/B6V14-48MPN3T-19S/2/e696034f9dc2c99356a49beeb111b91d)
- 995 Samson, M., 1993. Modelling of knots in logs. *Wood Science and Technology*
996 27 (6), 429–437.
- 997 Samson, M., Bindzi, I., Kamoso, L., 1996. Mathematical representation of
998 knots in tree trunks. *Canadian Journal of Forest Research* 26 (2), 159–165.
- 999 Sanderson, C., 2010. Armadillo: An open source C++ linear algebra library
1000 for fast prototyping and computationally intensive experiments. Technical
1001 Report, NICTA, <http://arma.sourceforge.net/>.
- 1002 Sarigul, E., Abbott, A. L., Schmoldt, D. L., 2003. Rule-driven defect de-
1003 tection in CT images of hardwood logs. *Computers and Electronics in*
1004 *Agriculture* 41, 101–119.
- 1005 Schad, K. C., Schmoldt, D. L., Ross, R. J., 1996. Nondestructive methods
1006 for detecting defects in softwood logs.
- 1007 Schmoldt, D. L., He, J., Abbott, A. L., 1998a. A comparison of several arti-
1008 ficial neural network classifiers for CT images of hardwood logs. In: *Engi-*

- 1009 neering, S.-T. I. S. f. O. (Ed.), Machine Vision Applications in Industrial
1010 Inspection VI. Vol. 3306. San Jose, California.
- 1011 Schmoldt, D. L., He, J., Abbott, A. L., 1998b. Classifying features in CT
1012 imagery: accuracy for some single and multispecies classifiers. In: The
1013 3rd International Seminar/Workshop on Scanning Technology and Image
1014 Processing on Wood. Skellefteå, Sweden.
- 1015 Schmoldt, D. L., Li, P., Abbott, A. L., 1996. A new approach to automated
1016 labeling of internal features of hardwood logs using CT images. Review
1017 of Progress in Quantitative Nondestructive Evaluation 15, 1883–1890, le
1018 prétraitement est bien détaillé.
- 1019 Seifert, T., Nickel, M., Pretzsch, H., 2010. Analysing the long-term effects of
1020 artificial pruning of wild cherry by computer tomography. Trees.
- 1021 Skovsgaard, J. P., 1988. Branch thickness in unthinned stands of Sitka spruce
1022 (*Picea sitchensis* (Bong.) Carr.). Scandinavian Journal of Forest Research
1023 3 (2).
- 1024 Som, S., Davis, J., Wells, P., Svalbe, I., 1993. Morphology methods for pro-
1025 cessing tomographic images of wood. In: Digital Image Computing: Tech-
1026 niques and Applications (DICTA). Sydney, Australia, pp. 564–571.
- 1027 Som, S., Svalbe, I., Davis, J., Grant, J., Gold, E., Tsui, K., Wells, P., 1995.
1028 Internal scanning of logs for grade evaluation and defect location. In: Dig-
1029 ital Image Computing: Techniques and Applications (DICTA). Brisbane,
1030 Australia, pp. 408–413.

- 1031 Taylor, F. W., Wagner, F. G., J., McMillin, C. W., Morgan, I. L., Hopkins,
1032 F. F., 1984. Locating knots by industrial tomography - A feasibility study.
1033 Forest Products Journal 34 (5), 42–46.
- 1034 Wei, Q., Chui, Y. H., Leblon, B., Zhang, S. Y., 2008a. Identification of log
1035 characteristics in computed tomography images using back-propagation
1036 neural networks with the resilient back-propagation training algorithm and
1037 textural analysis: Preliminary results. Wood and Fiber Science 40 (4), 620–
1038 633.
- 1039 Wei, Q., Chui, Y. H., Leblon, B., Zhang, S. Y., 2009. Identification of selected
1040 internal wood characteristics in computed tomography images of black
1041 spruce: a comparison study. Journal of Wood Science 55 (3), 175–180.
- 1042 Wei, Q., Leblon, B., Chui, Y. H., Zhang, S. Y., 2008b. Identification of
1043 selected log characteristics from computed tomography images of sugar
1044 maple logs using maximum likelihood classifier and textural analysis. Holz-
1045 forschung 62 (4), 441–447.
- 1046 Weiskittel, A. R., Seymour, R. S., Hofmeyer, P. V., Kershaw, Jr., J. A.,
1047 2010. Modelling primary branch frequency and size for five conifer species
1048 in Maine, USA. Forest Ecology and Management 259 (10), 1912–1921.
- 1049 Wells, P., Som, S., Davis, J., 1991. Automated feature extraction from to-
1050 mographic images of wood. In: Digital Image Computing: Techniques and
1051 Applications (DICTA). Melbourne, Australie.
- 1052 Zhu, D. P., Beex, A. A. L., 1994. Robust spatial autoregressive modeling

- 1053 for hardwood log inspection. *Journal of Visual Communication and Image*
1054 *Representation* 5 (1), 41–51.
- 1055 Zhu, D. P., Connors, R. W., Araman, P. A., 1991a. 3-D signal processing
1056 in a computer vision system. In: *International Conference on Systems*
1057 *Engineering*. Fairborn, Ohio, USA.
- 1058 Zhu, D. P., Connors, R. W., Araman, P. A., 1991b. CT image sequence
1059 processing for wood defect recognition. In: *The Twenty-third Southeastern*
1060 *Symposium on System Theory*. Columbia, South Carolina.
- 1061 Zhu, D. P., Connors, R. W., Lamb, F., Araman, P. A., 1991c. A computer
1062 vision system for locating and identifying internal log defects using CT
1063 imagery. In: *Fourth International Conference on Scanning Technology in*
1064 *the Wood Industry*. Burlingame, California.
- 1065 Zhu, D. P., Connors, R. W., Schmoldt, D. L., Araman, P. A., 1991d. CT im-
1066 age sequence analysis for object recognition - A rule-based 3-D computer
1067 vision system. In: *International Conference on Systems, Man, and Cyber-*
1068 *netics "Decision Aiding for Complex Systems"*. Charlottesville, Virginia.
- 1069 Zhu, D. P., Connors, R. W., Schmoldt, D. L., Araman, P. A., 1996. A proto-
1070 type vision system for analyzing CT imagery of hardwood logs. In: *IEEE*
1071 *Transactions on Systems, Man, and Cybernetics—Part B*. Vol. 26.
- 1072 Zuur, A. F., Ieno, E. N., Elphick, C. S., 2010. A protocol for data exploration
1073 to avoid common statistical problems. *Methods in Ecology and Evolution*
1074 1 (1), 3–14.

1075 **Acknowledgement**

1076 We would like to thank the people at the Ets. Siat-Braun who graciously
1077 supplied the beam samples, and Françoise Huber and Marie-Christine Trouy-
1078 Triboulot for the identification of the species.

Table 1: Upper bounds for the three criteria that were used for each validation data set. They were computed from the corresponding calibration data set of the cross-validation approach

Validation data set	Species	$n_{calibration}$	Inclination ($^{\circ}$)	Elongation	RDA ($^{\circ}$)
Beam #1	fir	298	52.1	0.26	16.3
Beam #2	fir	273	48.2	0.26	15.3
Beam #3	fir	290	54.0	0.23	15.0
Beam #4	fir	268	57.5	0.25	17.0
Beam #5	spruce	276	53.0	0.26	16.8
Beam #6	spruce	297	53.5	0.23	15.5
Beam #7	spruce	305	53.4	0.24	15.4

Table 2: Detection rates for each validation data set and for the whole data set

Validation data set	Number of manually measured knots	Number of automatically detected knots		Detection rate ^a (%)
		manually measured	not measured	
Beam #1	39	39	24	100
Beam #2	70	64	16	91
Beam #3	63	49	15	78
Beam #4	92	73	8	79
Beam #5	59	55	28	93
Beam #6	50	46	28	92
Beam #7	55	39	30	71
All beams	428	365	149	85

^aNumber of automatically detected knots that were measured divided by the number of manually measured knots

Table 3: Accuracy of automatic measurements for each validation data set

Variable of interest	Validation data set	n	R ²	RMSE	Mean error	SD error
Inclination (°)	Beam #1	39	0.98	4.5	-3.6	2.7
	Beam #2	64	0.87	4.2	2.1	3.6
	Beam #3	49	0.82	4.0	1.5	3.7
	Beam #4	73	0.75	2.6	1.2	2.3
	Beam #5	55	0.87	4.5	0.2	4.6
	Beam #6	46	0.87	6.9	-5.8	3.8
	Beam #7	39	0.90	4.5	-3.2	3.2
Maximum diameter (mm)	Beam #1	39	0.91	2.4	-1.6	1.7
	Beam #2	64	0.91	3.2	-2.4	2.2
	Beam #3	49	0.89	3.1	-2.3	2.1
	Beam #4	73	0.94	2.9	-1.4	2.6
	Beam #5	55	0.87	2.7	-0.8	2.6
	Beam #6	46	0.88	5.3	-2.9	4.5
	Beam #7	39	0.68	4.4	-1.3	4.2
Length (cm)	Beam #1	39	0.97	0.9	-0.6	0.7
	Beam #2	64	0.27	5.2	-3.4	3.9
	Beam #3	49	0.63	3.7	-2.4	2.8
	Beam #4	73	0.42	3.4	-2.0	2.7
	Beam #5	55	0.57	4.5	-2.5	3.8
	Beam #6	46	0.54	3.4	-2.0	2.8
	Beam #7	39	0.74	2.2	-0.7	2.1
Volume (cm ³)	Beam #1	39	0.97	6.5	3.2	5.7
	Beam #2	64	0.95	5.8	-2.9	5.1
	Beam #3	49	0.88	7.8	-2.8	7.3
	Beam #4	73	0.92	15.1	2.9	15.0
	Beam #5	55	0.88	11.8	3.1	11.5
	Beam #6	46	0.96	17.0	8.0	15.2
	Beam #7	39	0.44	20.0	9.2	18.0

1079 **List of Figures**

1080 1 General view of the scanned beams with the manual measure-
1081 ments. *Each beam was scanned in two 1.5-m length sections*
1082 *that are merged in the view. The beams are orientated accord-*
1083 *ing to their position in the standing tree based on the counting*
1084 *of annual growth rings. 53*

1085 2 Illustration of the 3D scan algorithm. At each step, only the
1086 two red slices need to be loaded into the system memory. The
1087 current voxel is represented in blue while the 17 neighbour
1088 voxels (part of the 26-neighbourhood) processed at each step
1089 are given in cyan. The previous processed slices are illustrated
1090 in grey, whereas the future ones are represented by empty
1091 transparent boxes. 54

1092 3 Illustration of the 3D distance map computed from a knot.
1093 *The resulting distance map is represented by gradient colours*
1094 *from red (nearest points) to blue (farthest points) on the cut-*
1095 *ting plane represented in (b). 55*

1096 4 Schematic view of the horizontal projection of a detected com-
1097 ponent and computation of starting point (SP), end point
1098 (EP), length, azimuth and radial deviation angle (RDA). . . . 56

1099	5	View of a whorl of beam #2. (a) Initial CT slice with manual measurements; (b) 3D view after knot segmentation; (c) Segmented slice with a specific colour for each component; (d) Convex hull of the segmented components. <i>Note that a component corresponding to the support table was detected but will be removed later when considering the knot criteria.</i>	57
1100			
1101			
1102			
1103			
1104			
1105	6	Knot connexion near the pith of beam #7. (a) Initial CT slice; (b) 3D view after knot segmentation; (c) Segmented slice with a specific colour for each component.	58
1106			
1107			
1108	7	Knot connexion due to wet areas in beam #4. (a) Initial CT slice; (b) 3D view after knot segmentation,; (c) Segmented slice with specific colour for each component.	58
1109			
1110			
1111	8	Number of knots from the seven beams that were manually measured and detected (grey), manually measured and not detected (red), not manually measured but detected (blue). . .	59
1112			
1113			
1114	9	Accuracy results for inclination, diameter, length and volume automatic measurements. <i>The black line corresponds to the $y=x$ axis.</i>	60
1115			
1116			
1117	10	Residuals for the knot length measurement as a function of the size of knots.	61
1118			

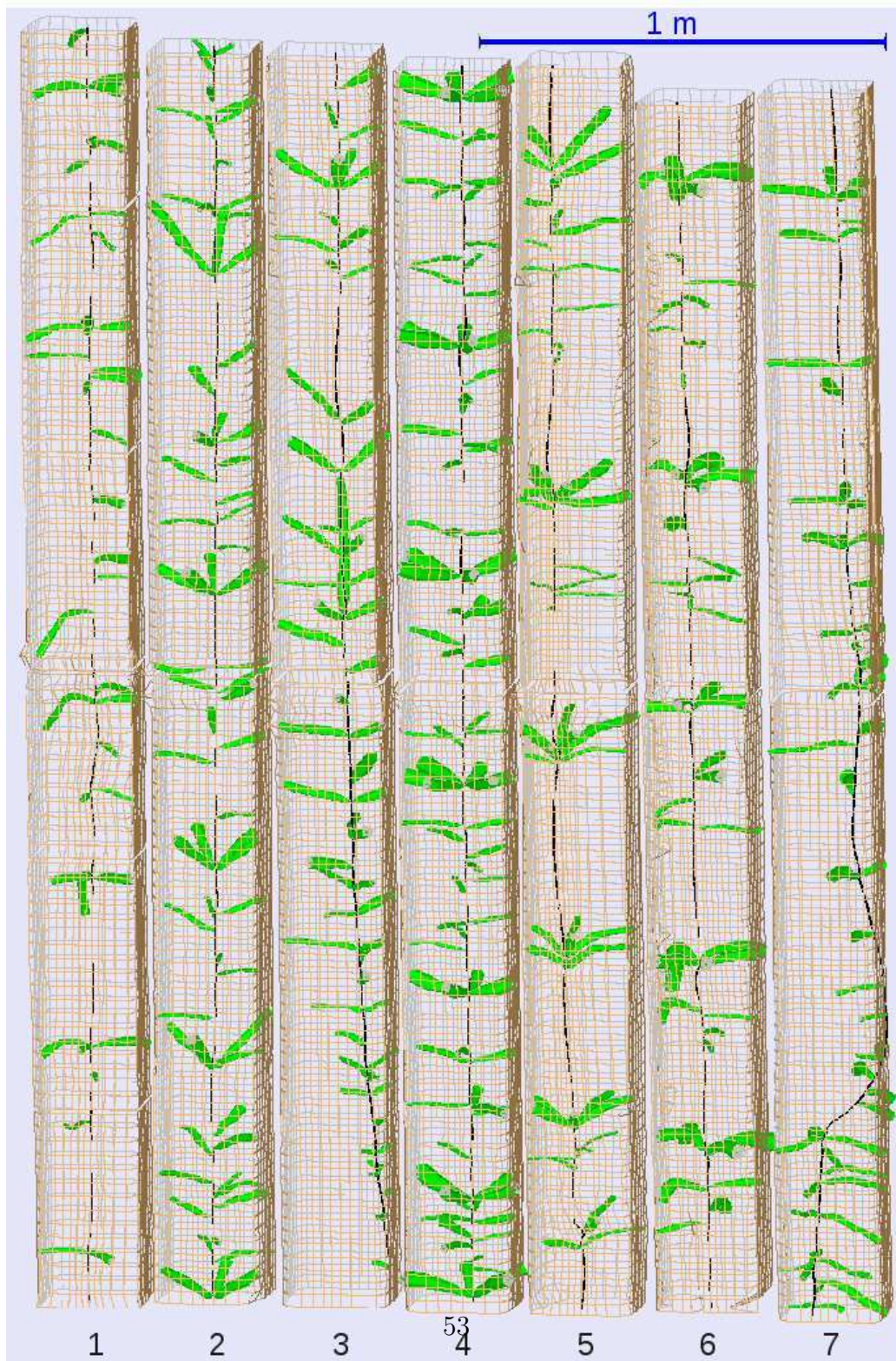


Figure 1: General view of the scanned beams with the manual measurements. *Each beam was scanned in two 1.5-m length sections that are merged in the view. The beams are orientated according to their position in the standing tree based on the counting of annual growth rings.*

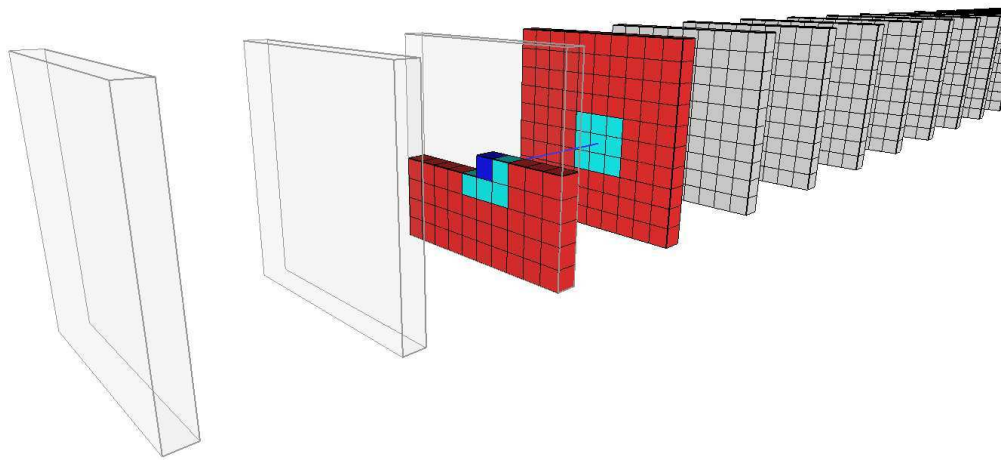


Figure 2: Illustration of the 3D scan algorithm. At each step, only the two red slices need to be loaded into the system memory. The current voxel is represented in blue while the 17 neighbour voxels (part of the 26-neighbourhood) processed at each step are given in cyan. The previous processed slices are illustrated in grey, whereas the future ones are represented by empty transparent boxes.

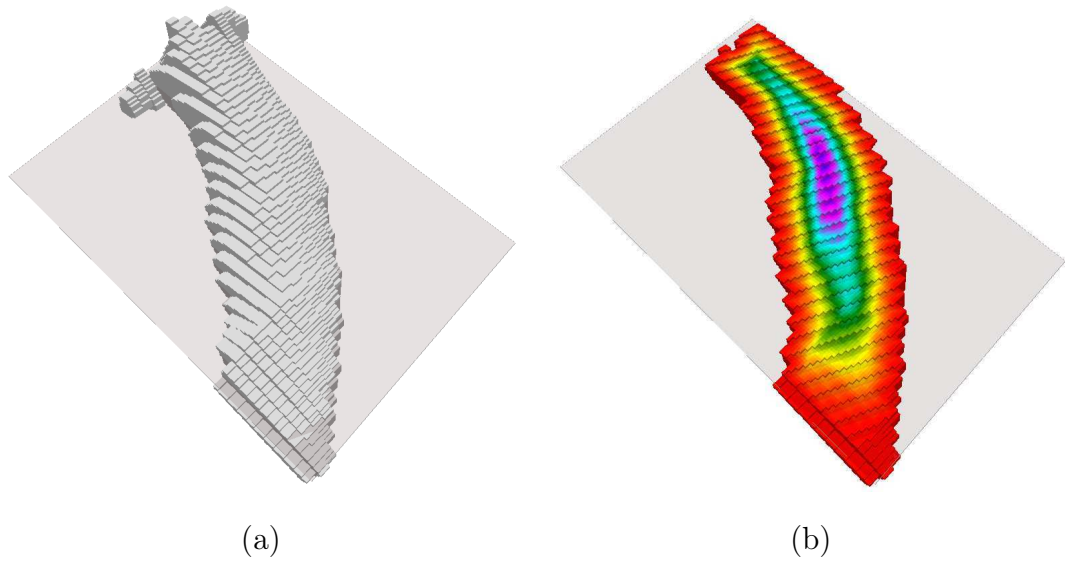


Figure 3: Illustration of the 3D distance map computed from a knot. *The resulting distance map is represented by gradient colours from red (nearest points) to blue (farthest points) on the cutting plane represented in (b).*

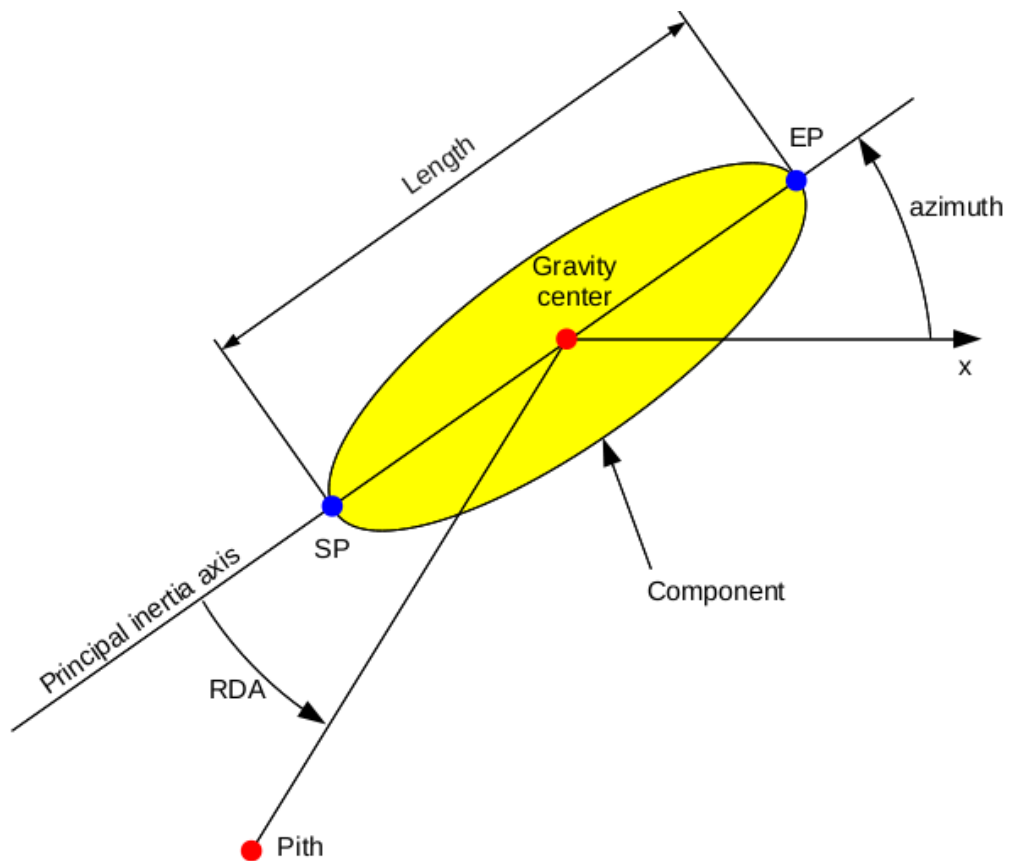


Figure 4: Schematic view of the horizontal projection of a detected component and computation of starting point (SP), end point (EP), length, azimuth and radial deviation angle (RDA).

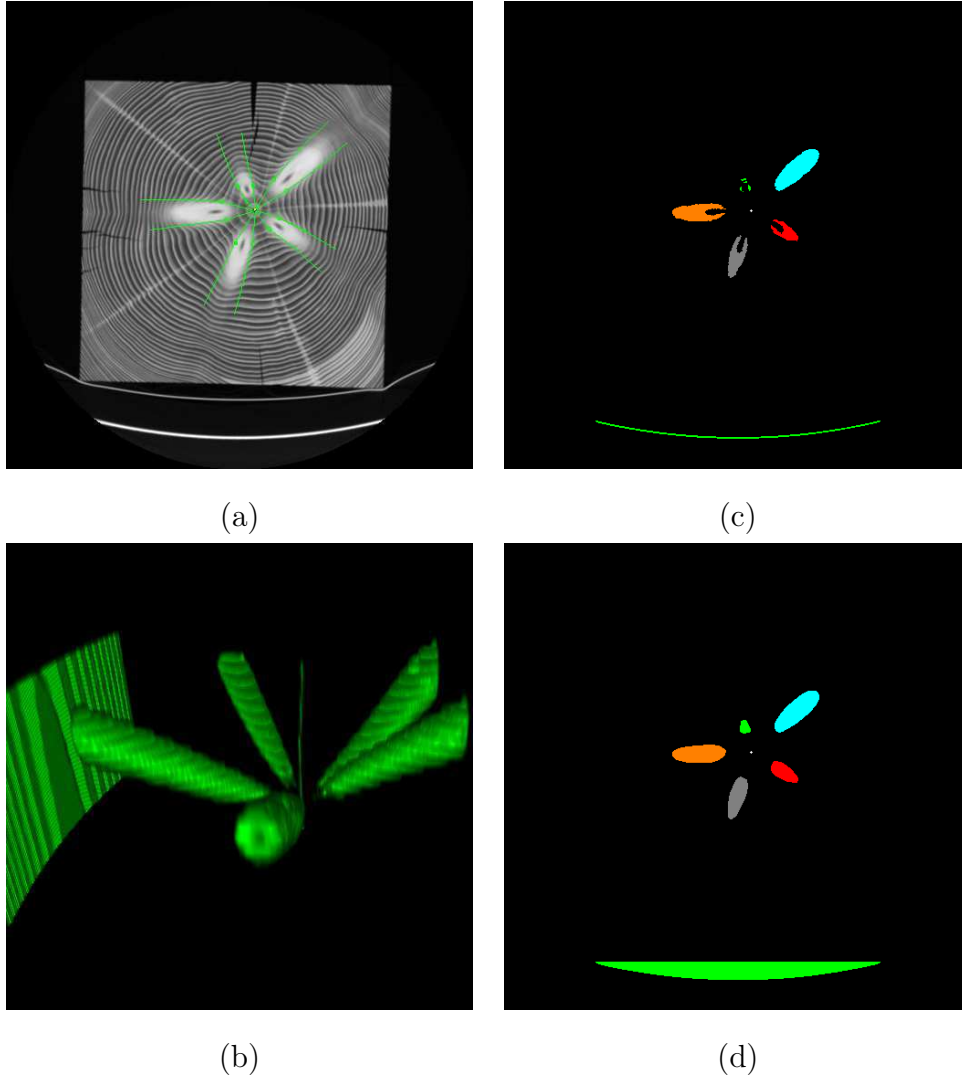


Figure 5: View of a whorl of beam #2. (a) Initial CT slice with manual measurements; (b) 3D view after knot segmentation; (c) Segmented slice with a specific colour for each component; (d) Convex hull of the segmented components. *Note that a component corresponding to the support table was detected but will be removed later when considering the knot criteria.*

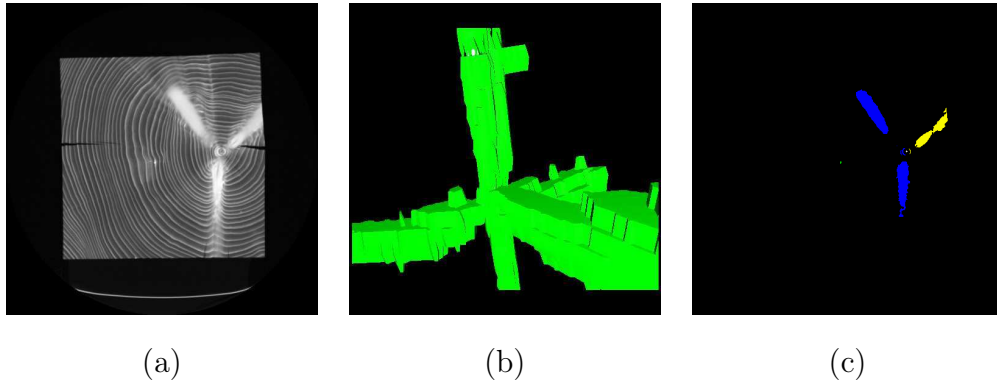


Figure 6: Knot connexion near the pith of beam #7. (a) Initial CT slice; (b) 3D view after knot segmentation; (c) Segmented slice with a specific colour for each component.

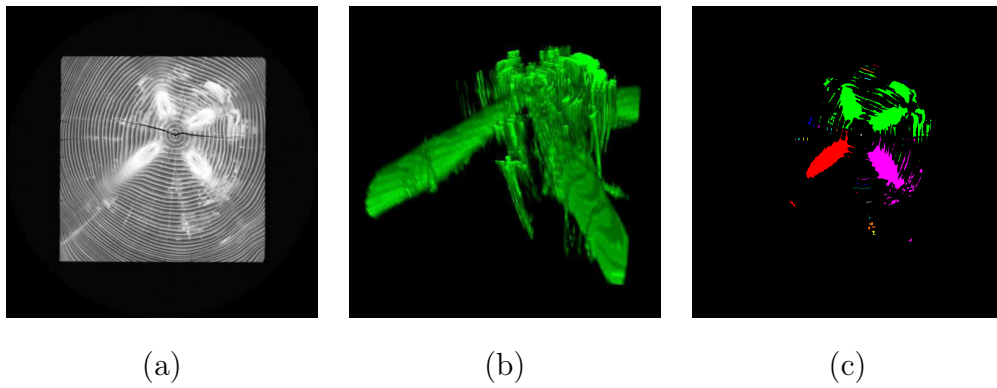


Figure 7: Knot connexion due to wet areas in beam #4. (a) Initial CT slice; (b) 3D view after knot segmentation,; (c) Segmented slice with specific colour for each component.

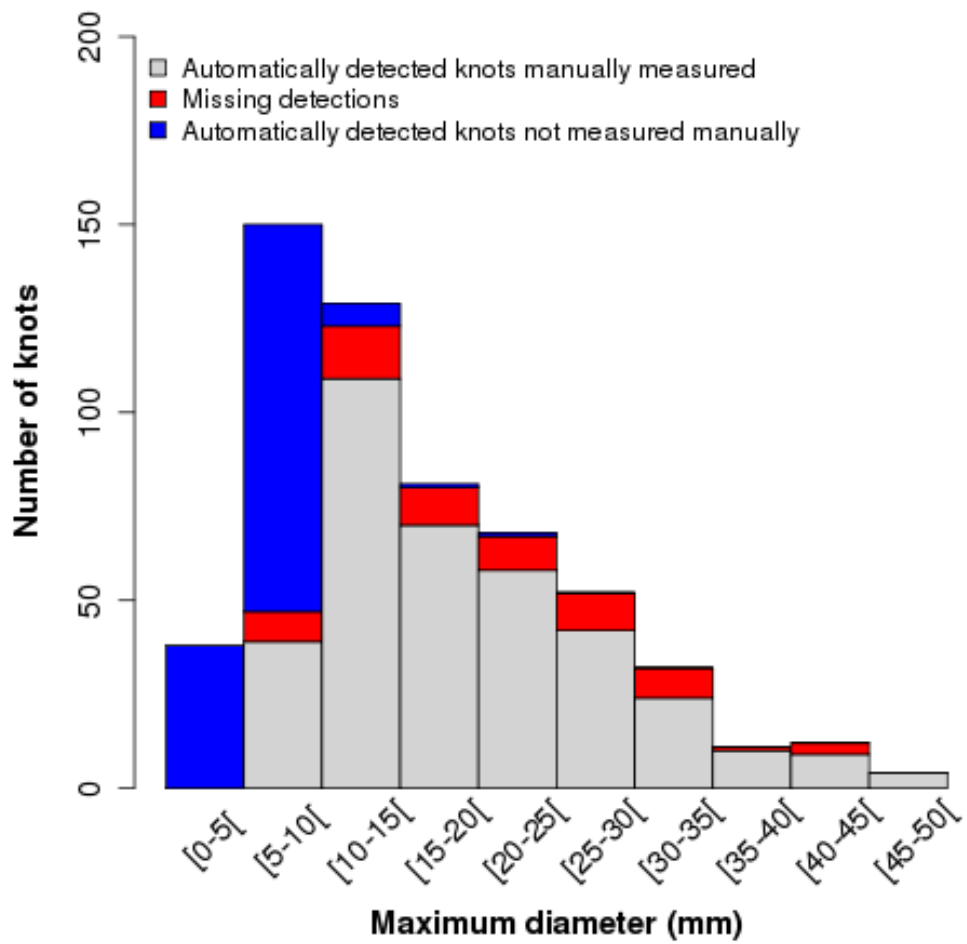


Figure 8: Number of knots from the seven beams that were manually measured and detected (grey), manually measured and not detected (red), not manually measured but detected (blue).

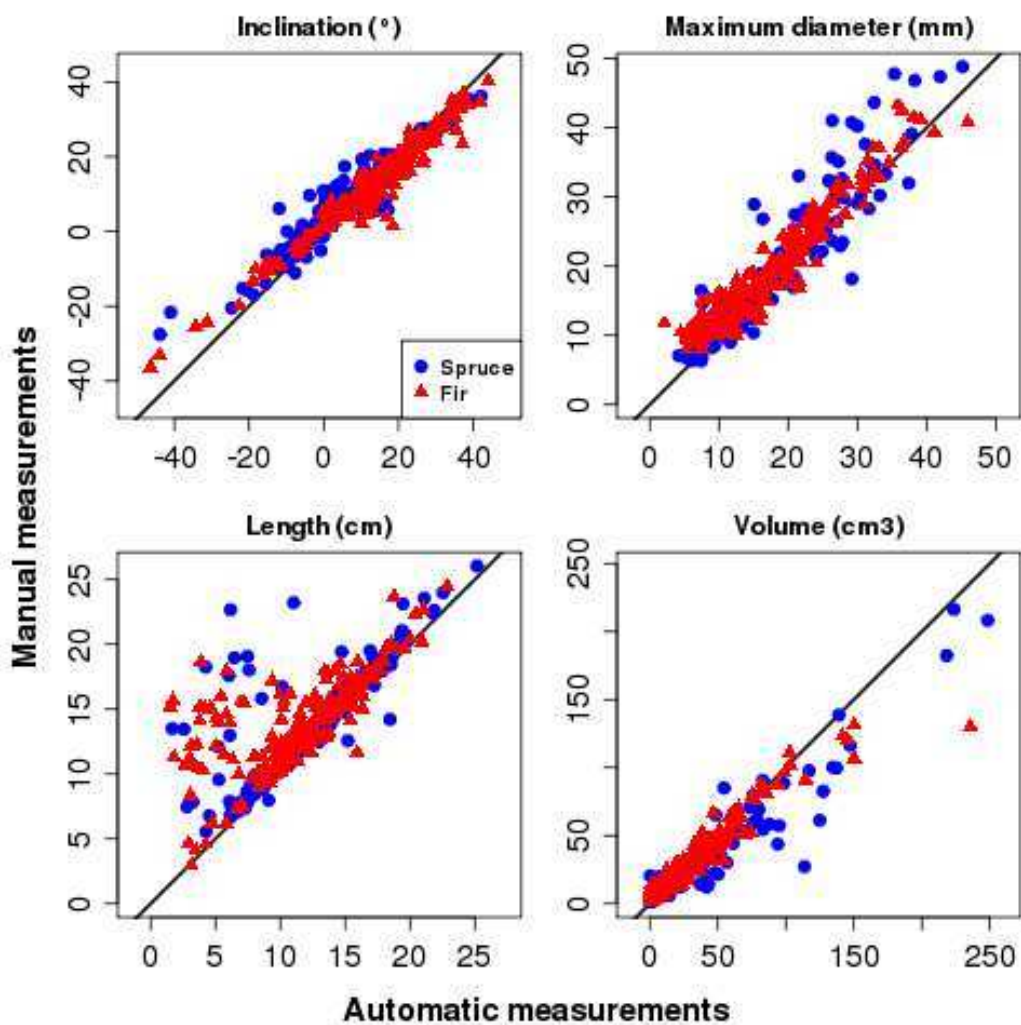


Figure 9: Accuracy results for inclination, diameter, length and volume automatic measurements. *The black line corresponds to the $y=x$ axis.*

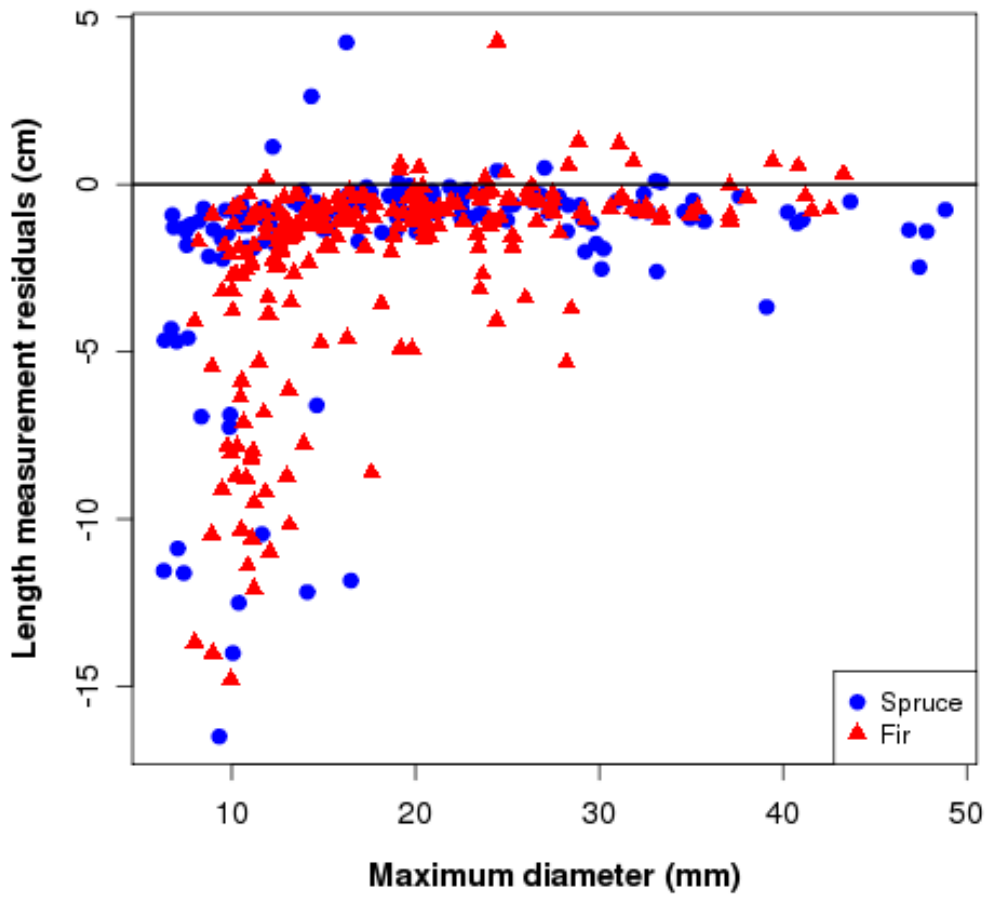


Figure 10: Residuals for the knot length measurement as a function of the size of knots.